Ultra-Wideband Coherent Processing

Kevin M. Cuomo, Jean E. Piou, and Joseph T. Mayhan

Lincoln Laboratory has developed an approach for estimating the ultra-wideband radar signature of a target by using sparse-subband measurements. First, we determine the parameters of an appropriate signal model that best fits the measured data. Next, the fitted signal model is used to interpolate between and extrapolate outside the measurement subbands. Standard pulse-compression methods are then applied to provide superresolved range profiles of the target. A superresolution algorithm automatically compensates for lack of mutual coherence between the radar subbands, providing the potential for ultra-wideband processing of real-world radar data collected by separate wideband radars. Because the processing preserves the phase distribution across the measured and estimated subbands, extended coherent processing can be applied to the ultra-wideband compressed radar pulses to generate superresolved radar images of the target. Applications of this approach to static test range and field data show promising results.

Lincoln Laboratory has played a major role in developing wideband radar systems. This development was motivated by the successful application of high-power instrumentation radars to research in ballistic missile defense and satellite surveillance. Today's wideband imaging radars perform real-time discrimination and target identification. Advanced signal processing methods have improved the resolution of processed radar return signals, further improving wideband-radar technology.

Figure 1 illustrates a ballistic missile defense environment that relies on accurate target identification and size-shape estimation, two capabilities critical to many areas of national defense. The primary goal of a defensive radar system is to intercept and destroy a threat target. This objective is complicated by the presence of many objects in the radar field of view, some purposefully designed to deceive radar discrimination algorithms. Decoys, for example, may have radar cross section (RCS) levels similar to those of the warhead, which makes robust target selection based solely on RCS levels difficult. Narrowband radars usually lack sufficient range resolution to allow a direct measurement of target length, although they are generally useful for tracking and coarse motion estimation. Unlike narrowband radars, wideband radars allow a much larger suite of target discrimination algorithms to be employed for real-time range-Doppler imaging and phase-derived range estimation.

Figure 2 illustrates a typical narrowband-radar and wideband-radar target response. The narrowband response indicates the position of the target as a whole with the peak RCS corresponding to the electromagnetic size of the target. The wideband response provides resolution within the target's range profile. Individual scattering centers are isolated into small range-resolution cells that provide a more direct measurement of the target's size and shape.

To achieve fine range resolution, wideband field radars utilize coded waveforms with large time-bandwidth products. Wideband chirp waveforms are commonly used because of their ease of generation and processing in the radar receiver. Mixing the radar return signals with a replica of the transmitted signal

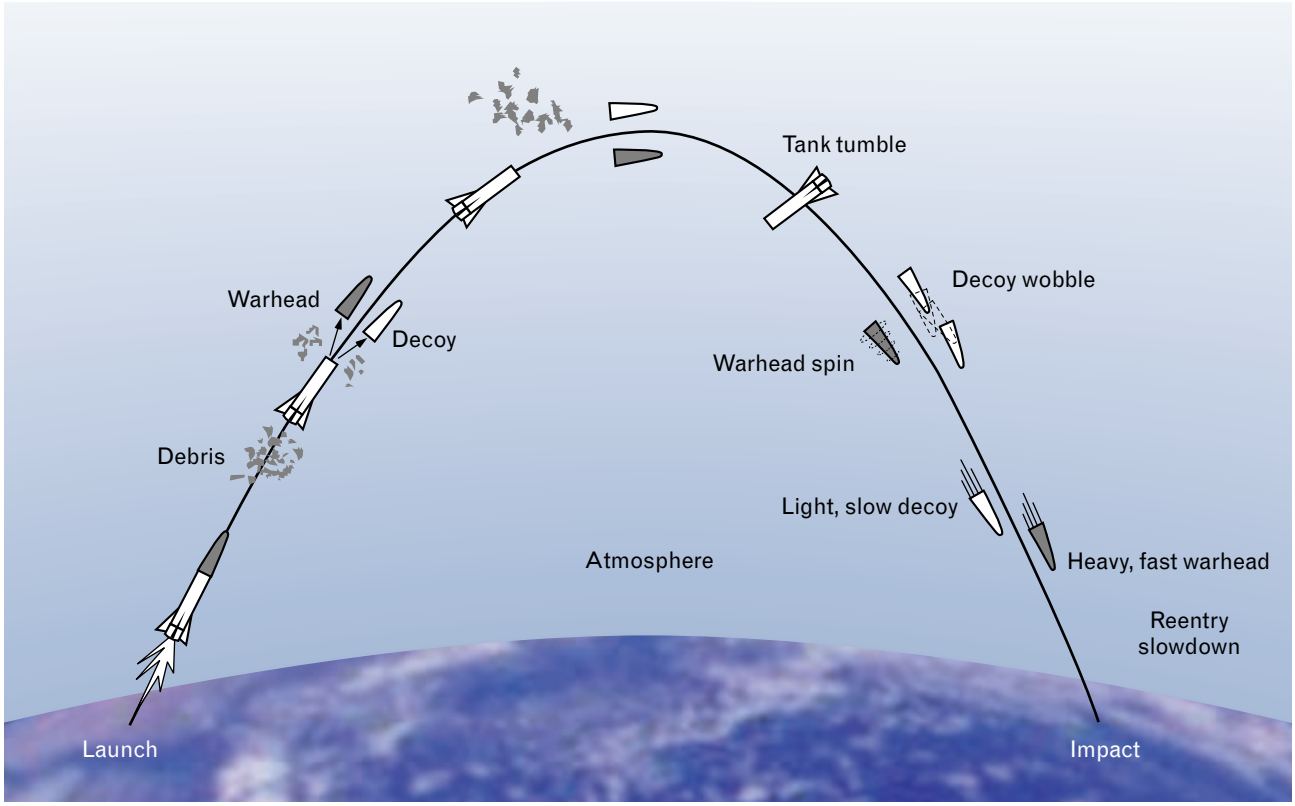

FIGURE 1. A typical ballistic missile defense environment, which demands accurate target identification and size-shape estimation. Shortly after launch, the warhead and decoy separate from the main body of the missile. Radar discrimination algorithms attempt to find the threat target by exploiting differences in size, shape, and motion dynamics between the warhead and nonthreatening objects in the radar's field of view.

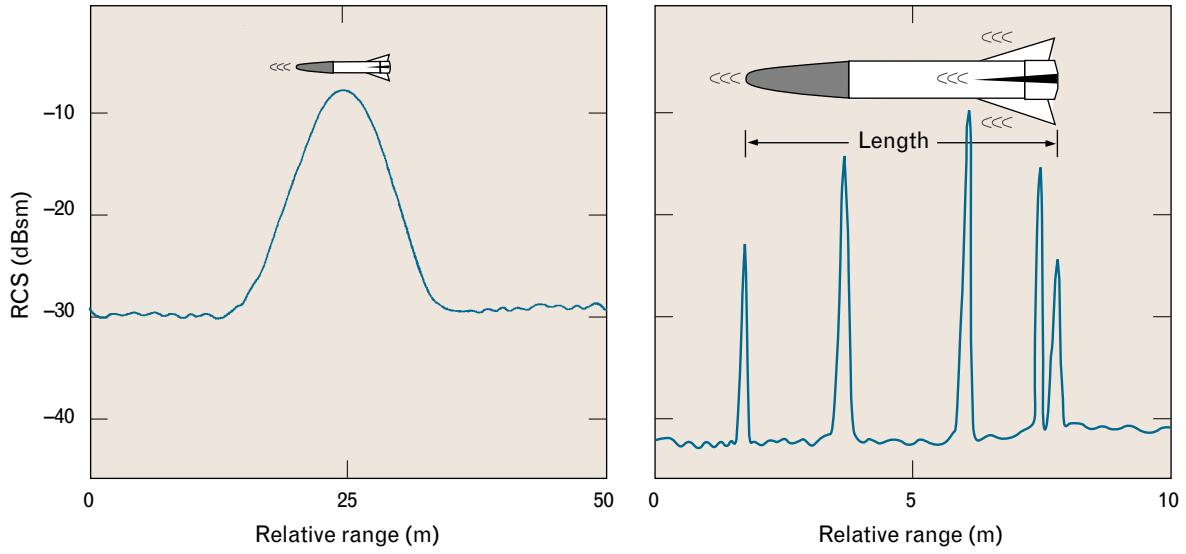

FIGURE 2. Comparison of target response—radar cross section (RCS) levels versus relative range—for a typical narrowband radar (left) and a wideband radar (right). The narrowband response can identify only the position of the target as a whole. The wideband response provides a direct measurement of individual scatterers within the target's length, permitting a much larger suite of target discrimination algorithms to be employed than with narrowband radars.

FIGURE 3. The Kiernan Reentry Measurement System (KREMS) facility located on Kwajalein Atoll in the central Pacific Ocean. The ALCOR C-band radar is located under the white radome in the lower left of the photograph. The millimeter-wave radar is located under the smaller white radome near the center.

produces a baseband signal with frequency components that are proportional to the relative range between scattering centers on the target. The baseband signal is sampled and Fourier-transformed to provide a range-resolved profile of the target. This process is called pulse compression. Properties of the compressed pulse, such as resolution and sidelobe levels, depend on the extent and shape of the window function applied to the baseband signal samples. The Fourier-theory relations define resolution to be inversely proportional to the total signal bandwidth. In accordance with this inverse relationship, the resolution of the radar improves as radar bandwidth increases.

Many wideband field radars operate on these basic principles. Figure 3 shows an aerial view of the Kiernan Reentry Measurement System (KREMS) facility located on Kwajalein Atoll in the central Pacific Ocean. This facility has been the most sophisticated and important wideband-radar research center in the United States for over thirty years [1]. The photograph depicts several wideband field radars, including the ALCOR C-band radar developed in 1970 for the purpose of wideband discrimination research. ALCOR utilizes a wideband chirp waveform with a bandwidth of 512 MHz to achieve a range-resolution capability of about 53 cm. Kwajalein's millimeter-wave radar can operate at the Ka-band and W-band, and is capable of a transmission bandwidth of 2000 MHz, providing an impressive 14-cm range-resolution capability. The United States also operates high-resolution wideband radars on ship platforms, such as COBRA JUDY. Figure 4 shows the COBRA JUDY S-band phased-array radar and the X-band dish-antenna radar.

Although the field radars mentioned above provide a high degree of range resolution, important target features are often much smaller than conventionally processed range-resolution cells. To improve the range resolution of a radar, we can increase the radar bandwidth or process the received signals with

FIGURE 4. The COBRA JUDY ship with a clear view of the S-band phased-array and X-band dish-antenna radars.

superresolution algorithms. Cost and design limitations are major drawbacks to increasing radar bandwidth. Because we want to obtain higher-resolution radar data without incurring significant hardware costs, we researched robust superresolution algorithms that can be applied to a wide range of real-world data sets.

In 1990, Lincoln Laboratory developed a superresolution algorithm that can significantly improve the range resolution of processed radar return signals. The algorithm, called bandwidth extrapolation (BWE) [2, 3], increases the effective bandwidth of a radar waveform by predicting the target's response at frequencies that lie outside the measurement bands. For radar applications, BWE typically improves the range resolution of compressed radar pulses by a factor of two to three. BWE often provides striking improvements in the quality of wideband-radar images. As an example, Figure 5(a) shows a radar image of a simulated three-point target without BWE processing applied. The resolution is insufficient to resolve the target points. Figure 5(b) shows the same target with BWE processing applied to the compressed radar pulses, first in the range dimension and then in cross-range. The BWE processed image is better resolved, allowing us to analyze and identify the target.

Although BWE improves resolution, the approach has the following inherent limitations. The algorithm is based on signal processing models that characterize a complex target as a collection of point scatterers, each having a frequency-independent scattering amplitude. BWE algorithms are often sufficient for typical wideband signal processing in which the waveforms have a small fractional bandwidth compared with the center frequency. Over ultrawide frequency bands in which the radar bandwidth is comparable to the radar center frequency, however, the scattering amplitude of the individual scattering centers can vary significantly with frequency. Spheres, edges, and surface joins are examples of realistic scattering centers that exhibit significant amplitude variations as a function of frequency. Ultra-wideband (UWB) signal models must be flexible enough to accurately characterize these non-pointlike scattering centers.

The ability to measure or estimate a target's UWB radar signature is useful for many radar-discrimination and target-identification applications. Not only is fine range resolution obtained, but the amplitude variations of isolated scattering centers are useful for identifying the type of scattering center. Many canonical scattering centers are known to exhibit f^{α}-type scattering behavior; e.g., the RCS of flat plates, singly curved surfaces (cone sections), and doubly curved surfaces (sphere) vary as f^2, f^1, and f^0, re-

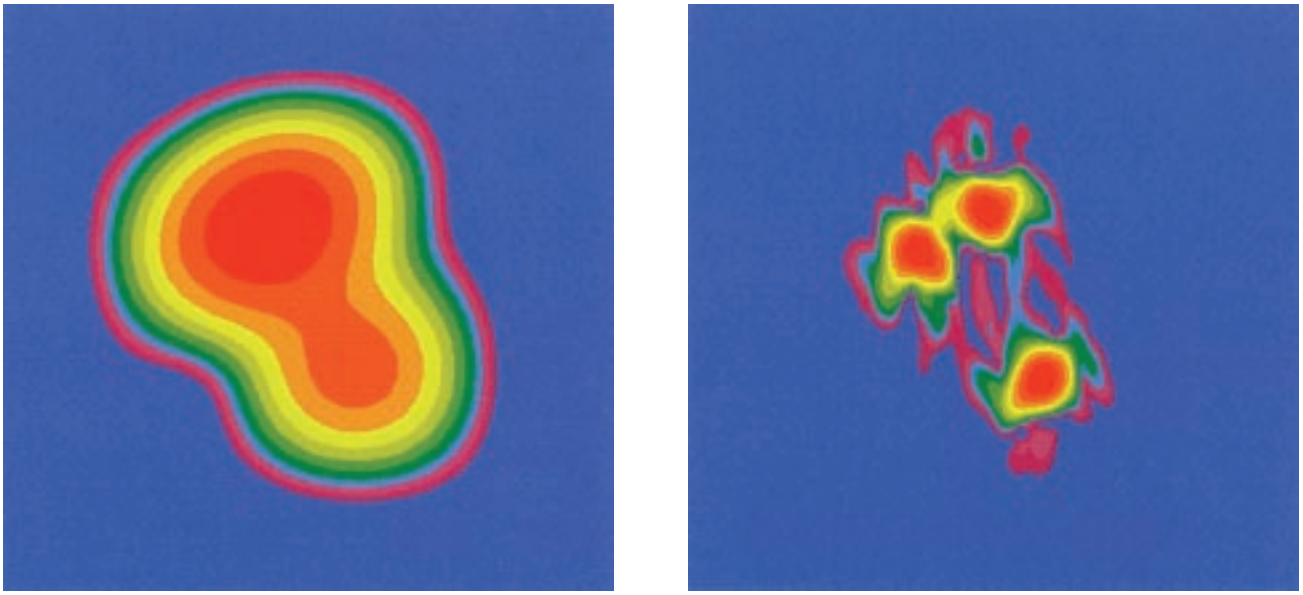

(a) (b)

FIGURE 5. Demonstration of bandwidth extrapolation (BWE) processing. (a) The three-point target image without BWE processing is not resolved well enough to identify the target. (b) The three-point target image with BWE processing allows us to identify and analyze the target.

spectively. The RCS of a curved edge varies as f^{-1}, whereas a cone vertex varies as f^{-2}. One goal of UWB processing is to detect these frequency-dependent terms in the measured data and to exploit them for scattering-type identification.

Building a field model of a true UWB radar can be expensive. A more practical approach is to use conventional wideband radars to sample the target's response over a set of widely spaced subbands, as illustrated in Figure 6. In this figure, the COBRA JUDY S-band and X-band radars are used to collect coherent target measurements over their respective widely spaced subbands. Coherently processing these subbands together makes it possible in principle to accurately estimate a target's UWB radar signature. This concept increases processing bandwidth and improves range-resolution and target-characterization capabilities.

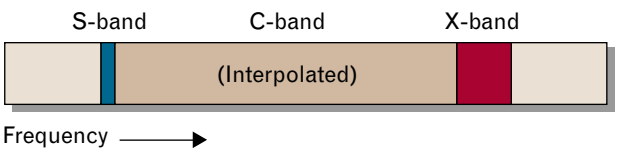

FIGURE 6. Ultra-wideband (UWB) processing concept applied to COBRA JUDY S-band and X-band wideband signature data. S-band and X-band measurements are coherently processed together to provide an interpolated estimate of a target's UWB radar signature.

To perform UWB processing, as illustrated in Figure 6, we must address a number of technical issues. First, we need to develop a robust signal processing method that compensates for the potential lack of mutual coherence between the various radar subbands. We must then fit an appropriate UWB signal model to the sparse-subband measurements. The fitted signal model must accurately characterize UWB target scattering and provide for meaningful interpolations or extrapolations outside the measurement subbands. In this article, we discuss our approach to UWB coherent processing, and then apply our UWB coherent processing algorithms to static-range data. We summarize the main results of this work and suggest some research strategies for the future.

UWB Coherent Processing

Figure 7 illustrates an overview of our approach to UWB coherent processing. An estimate of the target's UWB radar signature is obtained by coherently combining sparse-subband measurements. While the figure illustrates UWB processing for only two sub-

bands, it is straightforward to apply this concept to an arbitrary number of subbands.

The illustrated process is divided into three steps:

1. Process multiband data samples from the in-phase (I) and quadrature (Q) channels to make the radar subbands mutually coherent.
2. Optimally fit an UWB all-pole signal model to the mutually coherent subbands. The fitted model is used to interpolate between and extrapolate outside the measurement bands.
3. Apply standard pulse-compression methods to the enlarged band of spectral data to provide a superresolved range profile of the target.

Step 1 is important when applying UWB processing to field data collected by separate wideband radars. Time delays and phase differences between the radars can make them mutually incoherent. To cohere the subbands, we fit an all-pole signal model to the spectral data samples in each subband and adjust the models until they optimally match. Corresponding corrections are then applied to the underlying data samples. This approach is based on the assumption that the target can be accurately characterized by a superposition of discrete scattering elements. This assumption is often valid for targets that are large with respect to radar wavelength [4–6].

In step 2, we fit a global UWB all-pole signal model to the mutually coherent subbands. We then use the model for interpolation and extrapolation purposes. All-pole models are well suited for UWB processing because they accurately characterize the target by a superposition of discrete scattering centers, each with its own frequency-dependent term. While all-pole models match best to signals that grow or decay exponentially with frequency, they can also accurately characterize f^{α} scattering behavior over finite bandwidth intervals.

In step 3, standard Fourier-based pulse-compression methods are used to generate a range-resolved profile of the target. Because the UWB process is fully coherent, superresolved radar images can also be generated by using standard techniques.

Mutual-Coherence Processing

UWB processing requires a consistent set of spectral signals in each subband; i.e., the all-pole models for

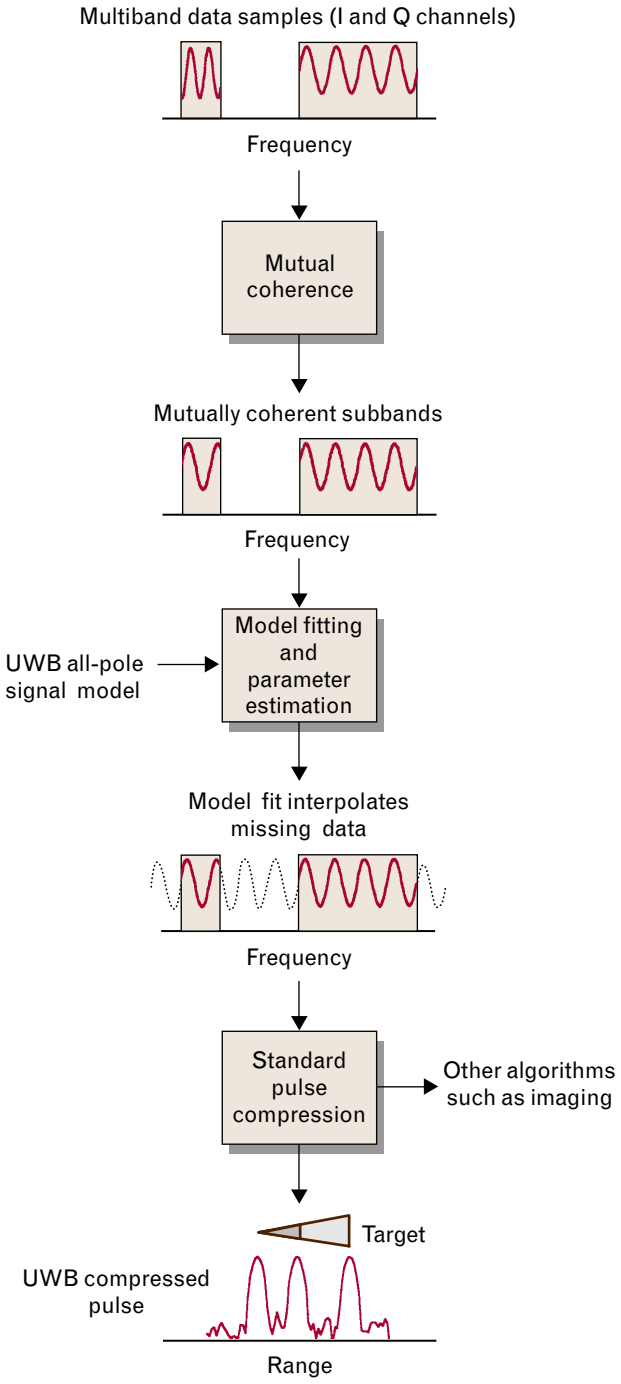

FIGURE 7. UWB process flow to estimate the target's UWB radar signature. Sparse multiband data samples for the in-phase (I) and quadrature (Q) channels are selected. Mutual-coherence processing allows two or more independent radar subbands to be used in the model fitting step that follows. An all-pole signal model is fitted to the sparse-subband data samples and used for interpolation and extrapolation outside the measurement bands. Standard pulse-compression methods are then applied to the UWB target data.

each subband must be consistent. This requirement is not an issue in multiband radar systems specifically designed to be mutually coherent. Mutual-coherence problems will most likely occur, however, when the subband measurements are collected by wideband radars operating independently. This section discusses a straightforward signal processing approach that can compensate for the lack of mutual coherence between any number of radar subbands. The technique allows us to apply UWB processing across a wider range of radar platforms used in the field.

For illustration purposes, we simulate the radar returns for a hypothetical target consisting of two discrete scattering centers. The scattering center closer to the radar has a scattering amplitude that decays with frequency, whereas the scattering center away from the radar has a scattering amplitude that grows with frequency. The simulated spectral signal samples s_n are given by

$$s_n = 4\left(\frac{f_n}{f_1}\right)^{-1} e^{i\pi n/4} + \left(\frac{f_n}{f_1}\right)^{1} e^{i\pi n/3} .$$

The frequency-sampled phase terms correspond to a scattering-center separation of 15 cm. White Gaussian noise is added to each signal sample and the signal-to-noise ratio is 20 dB.

We assume that only two subbands are available for coherent processing of the noisy s_n signal samples illustrated in Figure 8(a). The s_n signal samples in the lower subband have been modulated by the function $e^{-i\pi n/9}$ to simulate the effects of mutual incoherence; i.e., the signal poles for the lower subband have been rotated 20° clockwise relative to the upper-subband signal poles. Figure 8(b) shows the corresponding compressed pulses, which do not line up because the subbands are not mutually coherent. In effect, mutual coherence is seen as a consequence of uncertainty in

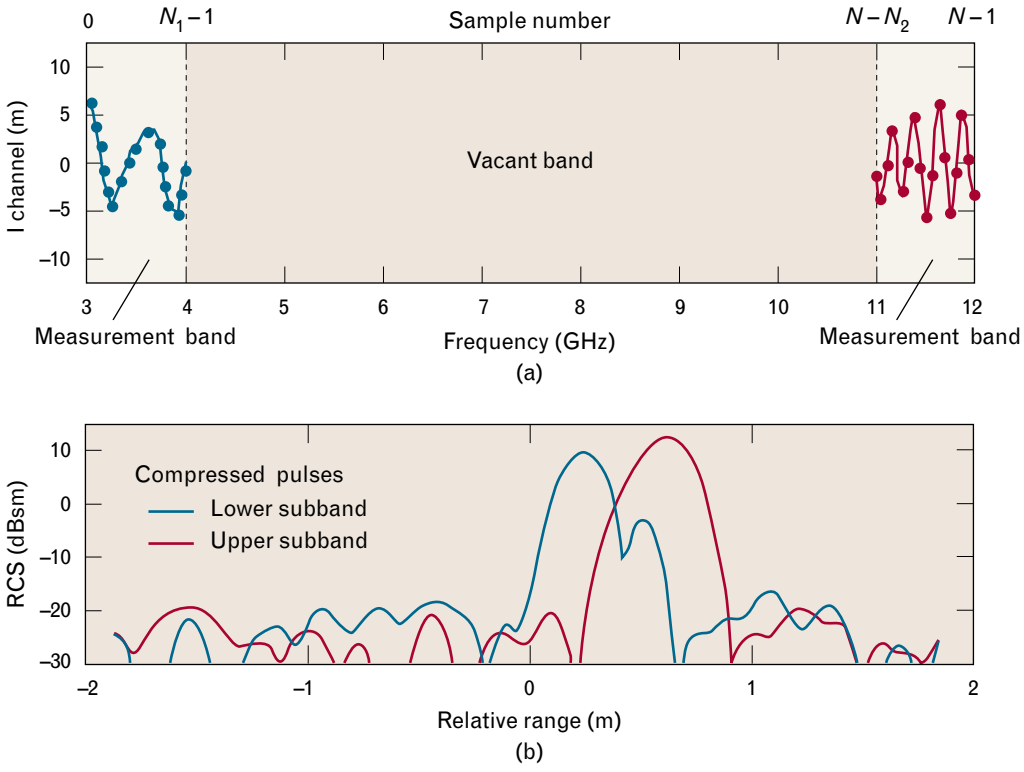

FIGURE 8. (a) Sparse multiband measurements of a target consisting of two closely spaced scattering centers. The amplitude of one scatterer (blue) decays with frequency, while the amplitude of the other scatterer (red) grows with frequency. The two subbands illustrated are not mutually coherent. For clarity, signals from only the I channel are shown. (b) The corresponding compressed pulses do not line up in range because the subbands are mutually incoherent.

position and time sequencing of the separate radars.

We begin the mutual-cohering process by modeling the spectral signals in each subband with a superposition of complex exponential functions. An all-pole signal model of the form

$$M(f_n) = \sum_{k=1}^{P} a_k p_k^n$$

is used for this purpose. As illustrated in Figure 8(a), the lower subband contains N_1 data samples, while the upper subband contains N_2 data samples. Thus the sample index n ranges from $n = 0, \ldots, N_1 - 1$ for the lower subband and from $n = N - N_2, \ldots, N - 1$ for the upper subband. The all-pole model parameters are physically meaningful. The number of scattering centers and their complex amplitudes are denoted by P and a_k, respectively. The poles p_k characterize the relative ranges and frequency decay of the individual scattering centers; the f^{α} frequency decay model indicated earlier is approximated by an exponential variation over the band of interest. The subbands can be mutually cohered by fitting a separate all-pole model to each subband and adjusting the models until they are consistent.

Our approach to all-pole modeling utilizes the singular-value decomposition of the forward-prediction matrix. Specifically, the forward-prediction matrix for the lower subband is given by

$$\mathbf{H}_1 = \begin{bmatrix} s_0 & s_1 & \cdots & s_{L-1} \\ s_1 & s_2 & \cdots & s_L \\ \vdots & \vdots & \vdots & \vdots \\ s_{N_1-L} & s_{N_1-L+1} & \cdots & s_{N_1-1} \end{bmatrix},$$

where L denotes the correlation window length and the s_n denote the frequency-domain radar measurements. The special form of matrix $\mathbf{H}_1$ is called a Hankel matrix, which is associated with the transient response of a linear-time-invariant system. Subspace decomposition methods exploit the eigenstructure of Hankel matrices to estimate the parameters of linear-time-invariant signal models [7]. Using a correlation window length $L = N_1/3$ generally provides for robust parameter estimates. Larger values of L can provide better resolution, but the estimates may not be as robust to noise. The forward-prediction matrix $\mathbf{H}_2$ for the upper subband, constructed in a similar way, is

$$\mathbf{H}_2 = \begin{bmatrix} s_{N-N_2} & s_{N-N_2+1} & \cdots & s_{N-N_2+L-1} \\ s_{N-N_2+1} & s_{N-N_2+2} & \cdots & s_{N-N_2+L} \\ \vdots & \vdots & \vdots & \vdots \\ s_{N-L} & s_{N-L+1} & \cdots & s_{N-1} \end{bmatrix}.$$

To estimate the all-pole model parameters for the lower and upper subbands, we apply the singular-value decomposition to $\mathbf{H}_1$ and $\mathbf{H}_2$, respectively, which decomposes $\mathbf{H}_1$ and $\mathbf{H}_2$ into the product of three matrices:

$$\mathbf{H}_1 = \mathbf{U}_1 \mathbf{S}_1 \mathbf{V}_1'$$

and

$$\mathbf{H}_2 = \mathbf{U}_2 \mathbf{S}_2 \mathbf{V}_2',$$

where the prime symbol denotes the Hermitian operator. The $\mathbf{S}$ matrices contain the singular values for the two subbands. The $\mathbf{U}$ and $\mathbf{V}$ matrices contain the corresponding eigenvectors. In particular, the columns of the $\mathbf{V}$ matrices correspond to the eigenvectors of the respective subband covariance matrices. By decomposing $\mathbf{H}_1$ and $\mathbf{H}_2$ in this way, we can estimate the all-pole model parameters for each subband with the following four-step process:

1. The singular-value matrices $\mathbf{S}_1$ and $\mathbf{S}_2$ are used to estimate the model orders P_1 and P_2 for the two subbands.
2. P_1 and P_2 are used to partition $\mathbf{V}_1$ and $\mathbf{V}_2$ into orthogonal subspaces: a signal-plus-noise subspace and a noise subspace. A modified root-MUSIC (multiple signal classification) algorithm described below is applied to estimate the signal poles for each subband.
3. The all-pole model amplitude coefficients a_k are determined by using a linear least-squares fit to the measured data.
4. The resulting subband signal models are adjusted to optimally match.

In step 1, the singular values in $\mathbf{S}$ are used to estimate appropriate model orders for the two subbands. The relatively large singular values in $\mathbf{S}$ correspond to

strong signal components, while the small singular values generally correspond to noise. For low noise levels, there is a sharp transition between the large and small singular values. The transition point can be used as an estimate of the model order. At higher noise levels the transition from large to small singular values is smooth, making accurate model-order estimation more difficult. The Akaike Information Criterion (AIC) [8, 9] and Minimum Description Length (MDL) [10, 11] are two model-order estimation methods that work well in these cases. Figure 9 shows the singular-value spectra for the two-subband data set in Figure 8. The AIC and MDL model-order estimates are both correctly equal to two.

Once the model orders P_1 and P_2 have been estimated, we proceed to step 2, in which the subspace decomposition properties of $\mathbf{V}_1$ and $\mathbf{V}_2$ are used to estimate the dominant signal poles for each subband. The matrices $\mathbf{V}_1$ and $\mathbf{V}_2$ are partitioned into orthogonal signal-plus-noise and noise subspaces,

$$\mathbf{V}_1 = \left[\mathbf{V}_1^{sn} \;\; \mathbf{V}_1^{n}\right]$$

and

$$\mathbf{V}_2 = \left[\mathbf{V}_2^{sn} \;\; \mathbf{V}_2^{n}\right].$$

The partitioning is performed so that $\mathbf{V}_1^{sn}$ and $\mathbf{V}_2^{sn}$ have P_1 and P_2 columns, respectively. The noise subspace matrices $\mathbf{V}_1^{n}$ and $\mathbf{V}_2^{n}$ have $L - P_1$ and $L - P_2$ columns, respectively. Pole estimates for each subband are obtained by employing a modified root-MUSIC algorithm. Matrices $\mathbf{A}_1$ and $\mathbf{A}_2$ are defined from the noise subspace vectors for each subband as

$$\mathbf{A}_1 = \mathbf{V}_1^{n}\mathbf{V}_1^{n'}$$

$$\mathbf{A}_2 = \mathbf{V}_2^{n}\mathbf{V}_2^{n'}.$$

We denote a_{1i} as the elements of the first row of $\mathbf{A}_1$ and b_{1i} as the elements of the first row of $\mathbf{A}_2$. These elements are used to form the polynomials $A_1(z)$ and $A_2(z)$ given by

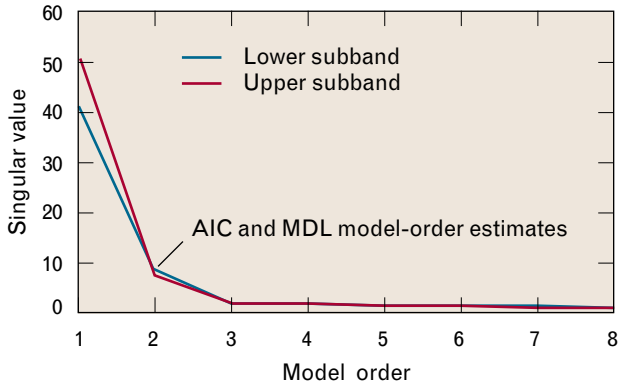

FIGURE 9. Singular-value spectra for the two-subband data set in Figure 8. The Akaike Information Criterion (AIC) and Minimum Description Length (MDL) model-order estimates are equal to two. The signal-to-noise ratio is 20 dB.

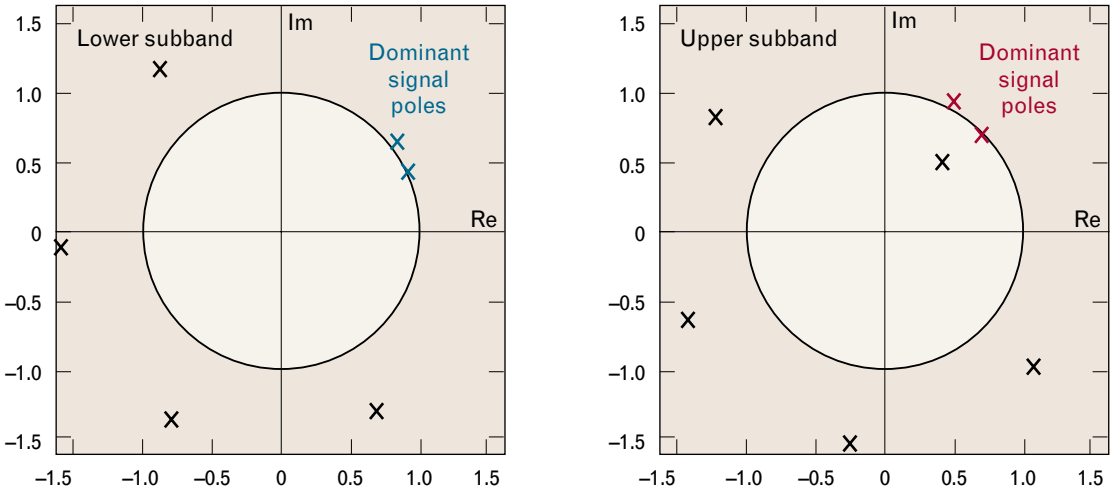

FIGURE 10. Pole estimates for the two-subband data set illustrated in Figure 8. The dominant signal poles in the lower and upper subbands are shown in blue and red, respectively.

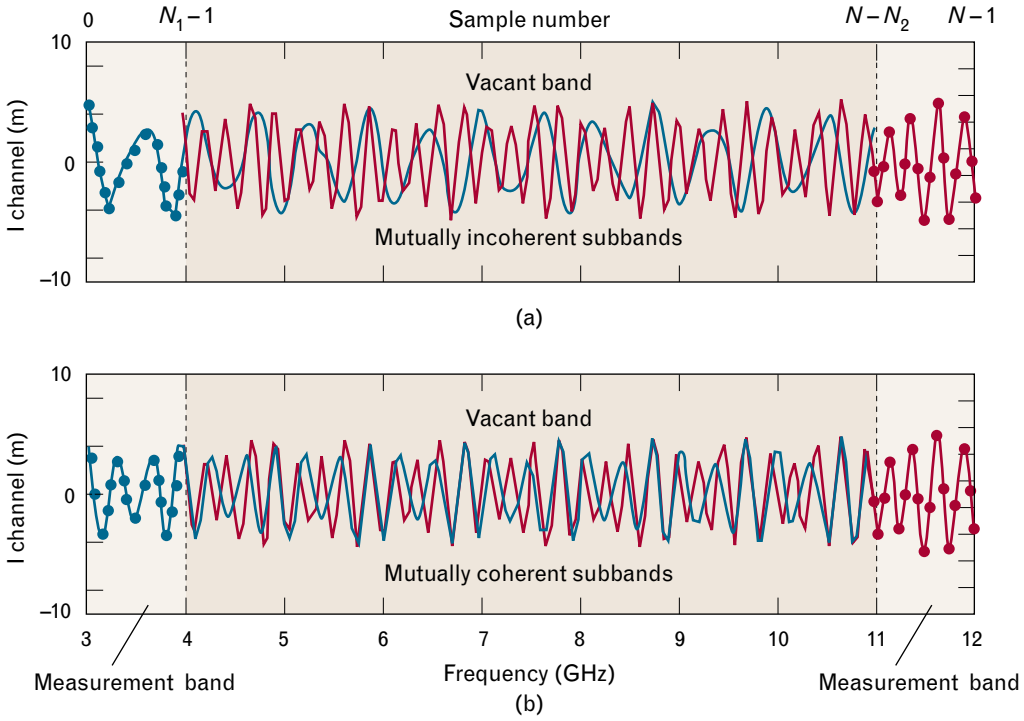

FIGURE 11. Mutual-coherence processing applied to the sparse-subband data set illustrated in Figure 8. Lower- and upper-subband signal models are shown before (a) and after (b) mutual-coherence processing. The mutually cohered signal models are consistent over much of the UWB processing interval.

$$A_1(z) = \sum_{i=1}^{L} a_{1i} z^{(i-1)}$$

$$A_2(z) = \sum_{i=1}^{L} b_{1i} z^{(i-1)} .$$

The roots of $A_1(z)$ and $A_2(z)$ correspond to pole estimates for bands 1 and 2, respectively.

This approach can be viewed as a variant of the traditional root-MUSIC algorithm described in Reference 12. Our approach has the important advantage of providing high-resolution pole estimates while eliminating the symmetric pole ambiguities that result from the traditional root-MUSIC approach.

Pole estimates can also be obtained by applying the spectral-estimation techniques described in References 13 through 19. In our algorithm, the pole estimates are obtained for each subband by applying the modified root-MUSIC algorithm to $\mathbf{V}_1^n$ and $\mathbf{V}_2^n$. The root-MUSIC algorithm finds poles corresponding to the signal vectors that are most orthogonal to the noise-subspace vectors. In general, the f^{α} variation of the signal model leads to poles that are displaced from the unit circle in the complex z-plane. Over each subband, however, the variation of f^{α} is small, so the dominant signals correspond to poles that lie close to the unit circle. After estimating model orders in step 1, we use the P_1 poles closest to the unit circle in step 2 to characterize the dominant lower-subband signals and the P_2 poles closest to the unit circle to characterize the dominant upper-subband signals.

Figure 10 shows the resulting pole estimates for the two-subband data set illustrated in Figure 8. The poles shown in blue and red are considered the dominant signal poles for the lower and upper subbands, respectively. Notice that a lack of mutual coherence prevents the signal poles in the lower subband from lining up with the signal poles in the upper subband.

In step 3, we estimate the all-pole amplitude coefficients a_k for the lower and upper subbands. An optimal set of amplitude coefficients can be found by solving a standard linear least-squares problem. Step 3

completes the all-pole modeling process for each subband. The lower- and upper-subband signal models are denoted by $M_1(f_n)$ and $M_2(f_n)$, respectively.

In step 4, the subband signal models $M_1(f_n)$ and $M_2(f_n)$ are adjusted until they optimally match. There are many ways to accomplish the match. A straightforward method involves modulating and phase-aligning the lower-subband signal model until it closely matches the upper-subband signal model. For example, the coherence function

$$C = \sum_{n=0}^{N-1} \left| AM_1(f_n)e^{i\Delta\theta n} - M_2(f_n) \right|^2$$

can be minimized with respect to the pole rotation angle $\Delta\theta$ and complex amplitude coefficient A. Another approach for matching the subband signal models is to find an appropriate rotation matrix that best aligns the signal subspace vectors contained in $\mathbf{V}_1$ and $\mathbf{V}_2$. Whichever method is employed, the subband model-alignment process tends to promote a strong sense of mutual coherence between the two subbands.

In Figure 11(a), we show the mutually incoherent subband signal models. In Figure 11(b), an optimal pole rotation angle $\Delta\theta^*$ and complex amplitude coefficient A^* were applied to the lower-subband signal model and corresponding data samples; i.e., the lower-subband data samples were replaced by mutually coherent data samples given by

$$\tilde{s}_n = s_n e^{i[\Delta\theta^* n + \arg(A^*)]}, \; n = 0, \ldots, N_1 - 1.$$

Although the two signal models in Figure 11(b) may not entirely agree, it is important to recognize that they have approximately the same signal poles. The corresponding all-pole model coefficients a_k, however, significantly differ. The lower subband favors the decaying signal component, whereas the upper subband favors the growing signal component.

UWB Parameter Estimation and Prediction

Once the radar subbands have been mutually cohered, a global all-pole signal model is optimally fitted to the measured data. Our approach determines the all-pole model parameters that minimize the cost function J given by

$$J = \sum_{\langle n \rangle} q_n \left| s_n - M(f_n) \right|^2.$$

The index n ranges over all of the available data samples. The coefficients q_n are used to weight the measurements appropriately. The function J measures the total weighted error between the model given by

$$M(f_n) = \sum_{k=1}^{P} a_k p_k^n$$

and the mutually coherent data samples in each subband.

Minimizing J with respect to the all-pole model parameters is a difficult nonlinear problem with no closed-form solution. Brute-force numerical solutions are not feasible because of the potentially large number of signal parameters that must be estimated. Figure 12 illustrates an alternative approach to solving this dilemma. Initial estimates of the all-pole model parameters are obtained by using the technique based on singular-value decomposition. These initial estimates are then iteratively optimized by using a standard nonlinear least-squares algorithm, such as the Newton-Raphson algorithm. (Detailed information about the Newton-Raphson algorithm can be found in many standard texts on numerical analysis [20].) If the initial parameter estimates are close to optimal, the standard nonlinear least-squares algorithm rapidly converges to the all-pole model parameters that minimize J.

Many methods will give an initial estimate of the global all-pole model parameters. One method is to construct the multiband prediction matrix given by

$$\mathbf{H} = \begin{bmatrix} \mathbf{H}_1 \\ \mathbf{H}_2 \end{bmatrix}.$$

The submatrices $\mathbf{H}_1$ and $\mathbf{H}_2$ correspond to the forward-prediction matrices for the lower and upper subbands, respectively. We call this approach subaperture processing because it combines the data samples from both subbands, providing the potential for robust parameter estimates from noisy data.

It is also possible to obtain multiband parameter

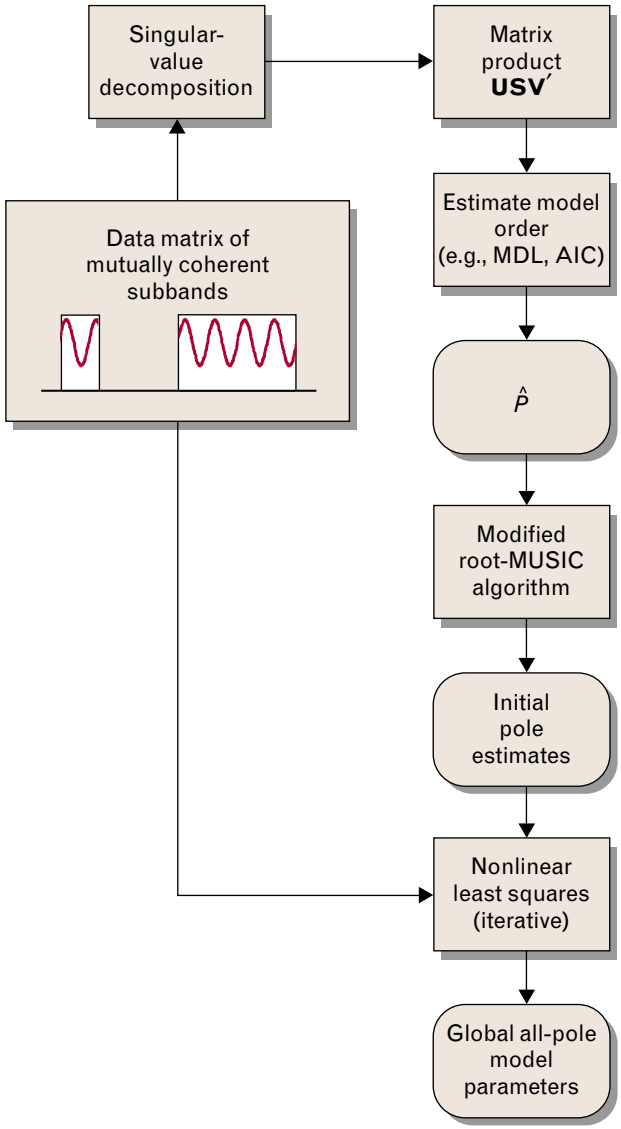

FIGURE 12. UWB parameter estimation. Initial parameter estimates are obtained by using a singular-value decomposition technique. These initial parameter estimates are iteratively optimized with a standard nonlinear least-squares algorithm.

estimates by allowing for cross-correlation between the subbands, i.e., by defining **H** as

$$\mathbf{H} = \left[\mathbf{H}_1\ \mathbf{H}_2\right].$$

We refer to this method as extended-aperture processing, which provides the potential for true UWB resolution. However, the resulting pole estimates are typically more sensitive to noise than those from subaperture processing. In principle, the two methods—subaperture processing and extended-aperture processing—can be combined to provide robust high-resolution estimates of the dominant signal poles. In both cases, multiband parameter estimates are obtained by decomposing **H** into the product of three matrices:

$$\mathbf{H} = \mathbf{USV}'.$$

An estimate $\hat{P}$ of the model order is obtained by applying the AIC or MDL techniques to the spectrum of singular values contained in **S**. For the sparse-subband data set illustrated in Figure 11(b), both the AIC and MDL model-order estimates are correctly equal to two. The model-order estimate is used to partition **V** into orthogonal signal-plus-noise and noise subspaces. Initial pole estimates are obtained by using the methods of a previous section, "Mutual-Coherence Processing," or any other superresolution spectral-estimation technique.

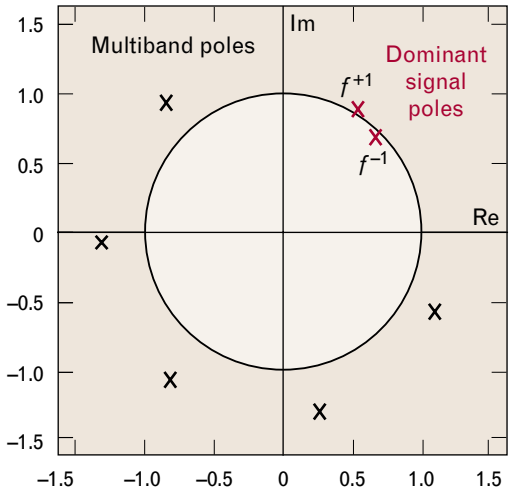

FIGURE 13. Multiband pole estimates for the mutually coherent subbands illustrated in Figure 11(b). The dominant signal pole inside the unit circle corresponds to the f^{-1} scattering center. The dominant signal pole outside the unit circle corresponds to the f^{+1} scattering center.

Figure 13 shows a plot of initial pole estimates for the sparse-subband data set illustrated in Figure 11(b). Including both $\mathbf{H}_1$ and $\mathbf{H}_2$ into the Hankel matrix correctly identifies both signal poles and associates them as f^{+1} and f^{-1} pole behavior. The two dominant signal poles are used to initialize the Newton-Raphson algorithm.

This algorithm uses the initial parameter estimates

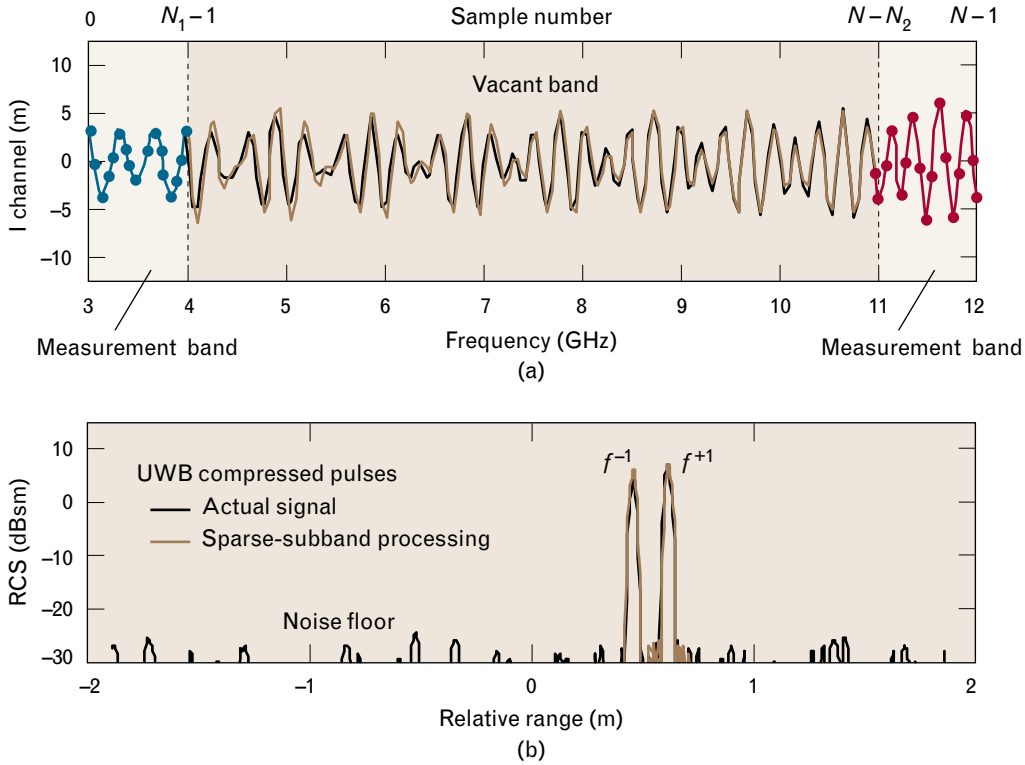

FIGURE 14. (a) Comparison between the fitted UWB signal model (brown curve) and truth (black curve). (b) Corresponding compressed pulses. The two scattering centers are well resolved with the UWB model closely matching truth.

to find the global all-pole model parameters a_k and p_k that locally minimize the cost function J. The model order P remains fixed during this iterative process and the algorithm typically converges to a local minimum of J in only a few iterations. We test the approach by optimally fitting a global all-pole signal model to the two subbands illustrated in Figure 11(b).

Figure 14(a) shows a comparison between the global all-pole signal model and the actual signal; the all-pole model agrees with the actual signal over the entire UWB frequency range. The corresponding compressed pulses are shown in Figure 14(b). The sparse-subband compressed pulse uses the mutually coherent radar measurements within the two subbands and the global all-pole model in the vacant band. With this approach, the two target points are well resolved and the estimated UWB response closely matches the actual signal.

This example also demonstrates the potential for using all-pole signal models to accurately characterize f^{α}-type scattering behavior over ultrawide processing bandwidths. In fact, the UWB pole estimates can be transformed into equivalent estimates of the α exponents for f^{α}-type signal models. We can always find an f^{α} function that best matches the exponential behavior of an UWB signal pole over a given frequency range. We can also derive an approximate analytical relationship between the pole magnitudes and the corresponding α exponents by matching the functions f^{α_k} and $|p_k|^n$ at the lowest and highest UWB frequencies. This relationship is given by

$$\alpha_k = \frac{(N-1)\log\left(|p_k|\right)}{\log\left[1+(N-1)\dfrac{df}{f_1}\right]}, \qquad (1)$$

where df and f_1 denote the spectral sample spacing and lowest UWB frequency, respectively. The constant N denotes the total number of UWB frequency samples. In the two-scattering-center example discussed previously, the two dominant signal poles p_1 and p_2 are given by

$$p_1 = 0.992e^{i\pi/4}$$
$$p_2 = 1.005e^{i\pi/3} .$$

By substituting these poles into Equation 1, we obtain an accurate estimate of the true α exponents used in the simulation. Thus the UWB pole locations provide information on scattering type. This information is useful for analyzing the details of targets with the viewpoint of constructing an accurate measurement-based model.

Static-Range Experiments

In the previous section, we presented the basic concepts behind our UWB processing algorithms. In this section, we utilize static-range data to demonstrate the applied aspects of UWB processing.

Figure 15 shows our target for the UWB processing demonstration—a monoconic model of a reentry vehicle with length of 1.6 m. The spherical nose tip of the reentry vehicle has a radius of 0.22 cm; the nose section is made from a solid piece of machined aluminum with two grooves and one seam. The first groove—approximately 3 mm deep and 6 mm wide—is located 22 cm from the reentry-vehicle nose tip. The second groove is approximately 2 mm deep and 4 mm wide, and is located 44 cm from the reentry-vehicle nose tip. The midbody of the reentry vehicle is made from a single sheet of rolled aluminum with one groove, one slip-on ring, and three seams. The aluminum slip-on ring (not shown in the photo) is approximately 5 mm thick and 10 mm wide, and is placed 1.4 m from the reentry-vehicle nose tip.

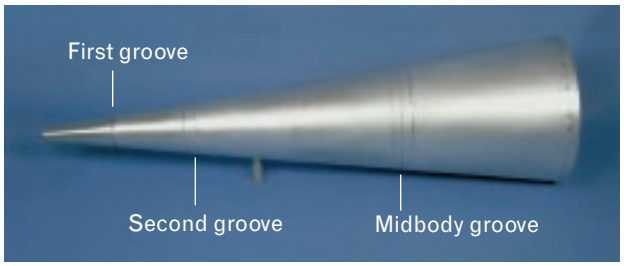

FIGURE 15. Test target for UWB processing experiments. This monoconic model of a reentry vehicle is 1.6 m long. The spherical nose tip has a radius of 0.22 cm. The nose section is made from a solid piece of machined aluminum with three grooves, two near the front of the model and one at midbody.

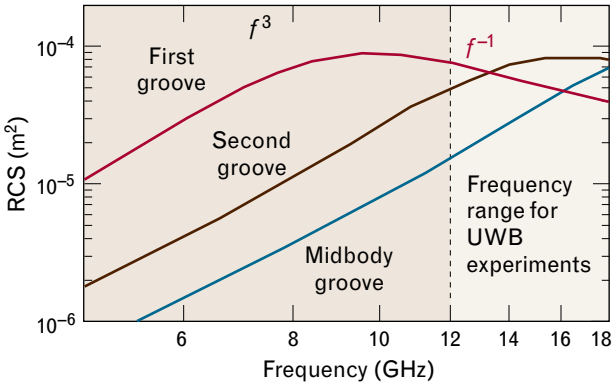

FIGURE 16. Moment-method RCS calculations for the three major grooves on the target, which was at a 20° aspect angle. All three grooves exhibit the expected f^3 scattering behavior at low frequencies, with break points that depend on the size of the groove.

The reentry vehicle shown in Figure 15 is ideal for UWB processing experiments because it has several scattering centers that exhibit significant RCS variations as a function of frequency. Figure 16 shows a moment-method RCS calculation for the three major grooves on the reentry vehicle. The grooves exhibit the expected f^3 scattering behavior at the low-frequency end of the spectrum, with break points that depend on the size of the groove.

The Lincoln Laboratory static-range radar facility was used to collect coherent radar measurements over a wide range of frequencies and viewing aspects of the target. Measurements were taken from 4.64 to 18 GHz in 40-MHz increments. The target viewing angles, relative to nose-on, ranged from –5° to 95° in 0.25° increments.

To demonstrate UWB processing, we focused on a segment of data collected in the 12-to-18-GHz region shown in Figure 16. Figure 17(a) shows an uncompressed radar pulse corresponding to an aspect angle of 20°. To test our UWB processing algorithms, we reduced the bandwidth of the uncompressed radar pulses to two 1.0-GHz-wide subbands, as illustrated in Figure 17(b). Figure 17(c) shows the compressed pulses for the two subbands and for the fullband data set. The bandwidth of the two subbands is insufficient to resolve many scattering centers on the target, while the fullband compressed pulse resolves all the significant scattering centers on the target. The pur-

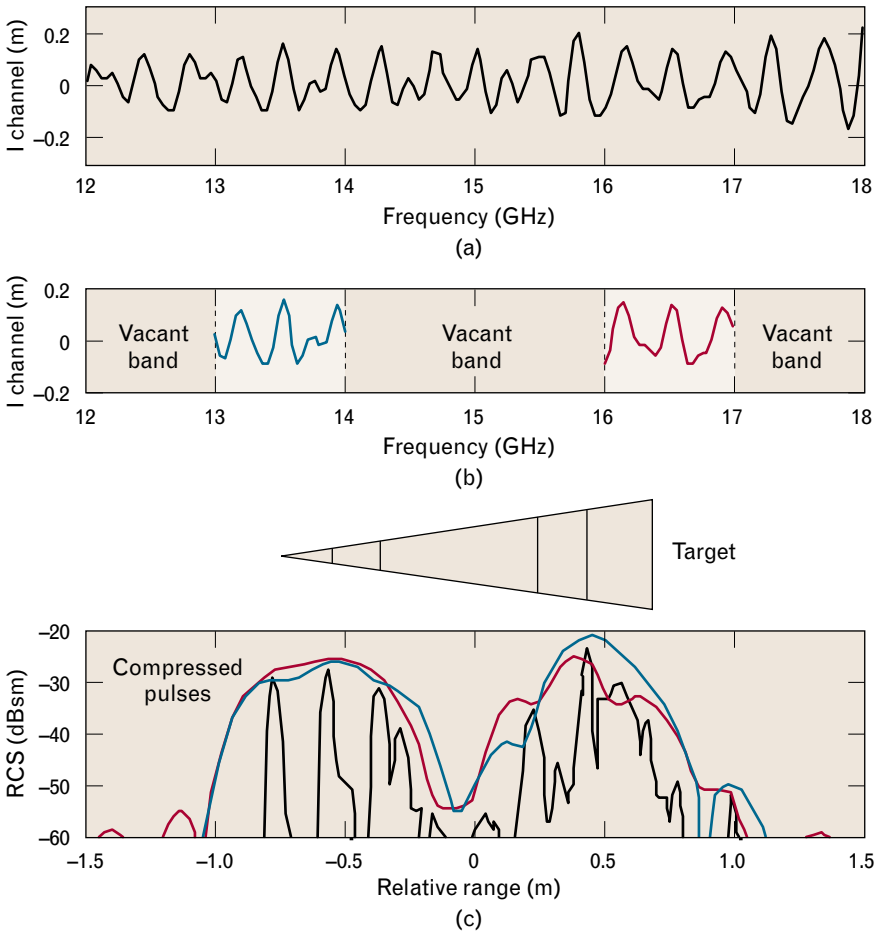

FIGURE 17. (a) Uncompressed radar pulse of the test target shown in Figure 15 with viewing aspect 20° from nose-on. (b) Sparse-subband measurements used to predict the target's response over the fullband from 12 to 18 GHz. (c) Compressed pulses for the sparse subbands and fullband data sets. The fullband compressed pulse (black) resolves all of the significant scattering centers on the target.

pose of this experiment was to use UWB processing to obtain a result highly consistent with the fullband result. We then demonstrated the ability to coherently process the subband measurements so that we can accurately estimate the target's UWB response.

Figure 18 shows the UWB pole estimates obtained by applying the sparse-subband spectral-estimation technique discussed earlier in the section entitled "UWB Coherent Processing." The pole locations are consistent with the physical scattering centers on the target. The pole corresponding to the nose-tip response is close to the unit circle, indicating it has a nearly constant RCS as a function of frequency. The grooves and slip-on ring have non-constant RCSs as a function of frequency; the corresponding poles are ei-

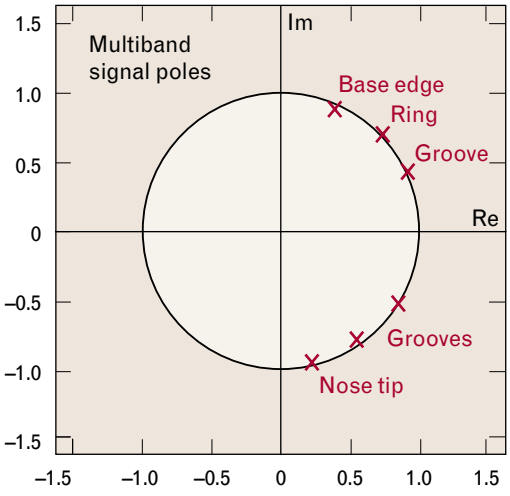

FIGURE 18. UWB pole estimates obtained by using the sparse-subband data set shown in Figure 17(b).

ther inside or outside the unit circle, as predicted by the moment-method RCS calculations in Figure 16.

Estimating the corresponding α exponents for these major scattering centers is straightforward—the magnitude of the signal poles is related to the α exponents via Equation 1. A more accurate relationship can be obtained by solving for the α exponents that produce the best match between the functions f^{α_k} and $|p_k|^n$ over the frequency range of interest, i.e., from 12 to 18 GHz. Using this approach, we estimated the α exponents for the first, second, and midbody grooves, respectively, on the reentry vehicle to be $\alpha_1 = -1.1$, $\alpha_2 = 2.3$, and $\alpha_3 = 2.9$. These estimates are consistent with the moment-method RCS calculations shown in Figure 16.

Figures 19(a) and 19(b) show comparisons between the estimated UWB target response and the true UWB radar measurements. The model and the measurements are in excellent agreement.

Because radar measurements were taken over a wide range of viewing aspects, we could generate two-dimensional radar images of the target. Figures 20(a) and 20(b) show the lower- and upper-subband images, respectively. The resolution is insufficient to resolve many of the scattering centers on the target. Figures 20(c) and 20(d) show the true and estimated UWB target images, respectively. All four images were generated by applying extended coherent processing [3] to the corresponding compressed pulses over the full range of available viewing aspects. We used target symmetry to process the data as if we had sampled a range of viewing aspects from –95° to 95°. The UWB images provide a clear picture of the target and show considerable detail. The sparse-subband image closely matches the fullband image and provides an accurate estimate of the locations and α exponents of the many realistic scattering centers on the target.

These experimental results suggest that UWB processing of sparse-subband measurements can signifi-

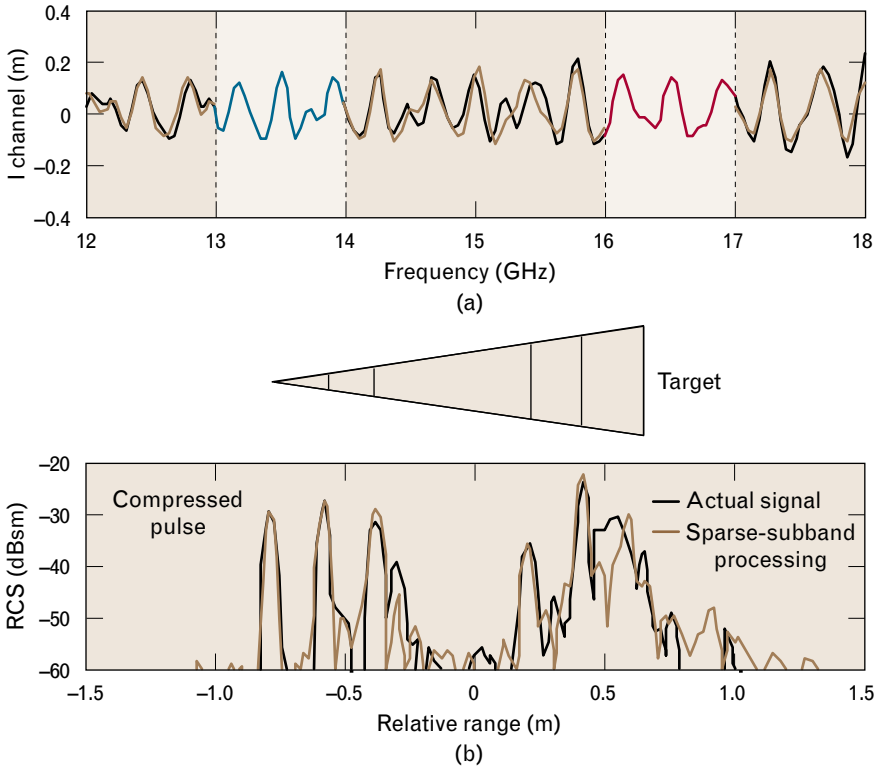

FIGURE 19. Comparisons between the estimated UWB target response and the true UWB radar measurements. (a) Uncompressed radar pulse for the prediction model (brown line) and the actual radar measurements (black line). (b) The corresponding compressed pulses that resolve the scattering centers on the target.

cantly improve range resolution and provide accurate characterizations of targets over ultrawide bandwidths. We are currently investigating fundamental limitations and practical payoffs of UWB processing.

Summary

This article presents an approach for accurately estimating a target's UWB radar signature from sparse-subband measurements. To apply this technology to field data, we developed an algorithm that could compensate for the potential lack of mutual coherence between the various radar subbands. Robust mutual-coherence processing was performed by optimally matching the all-pole signal models for each subband. With the radar subbands mutually cohered, a single UWB all-pole signal model was optimally fit-

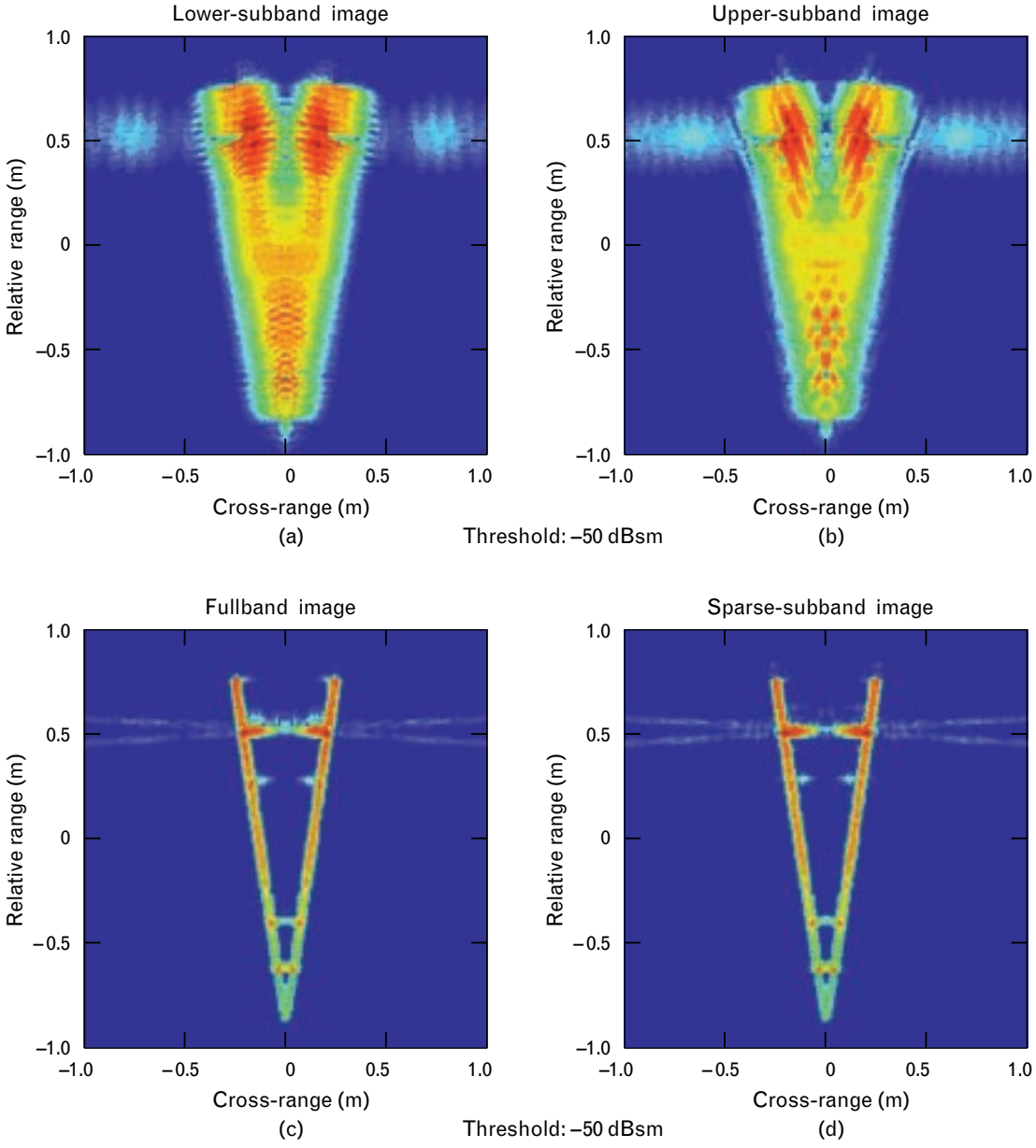

FIGURE 20. Comparison of two-dimensional radar images. The upper left and right images show the lower- and upper-subband images, respectively. The fullband image in the lower left uses actual radar measurements over the full 12-to-18-Ghz frequency range. The sparse-subband image in the lower right uses the sparse-subband measurements with UWB prediction.

ted to the available data. The fitted model was used to interpolate between and extrapolate outside the measurement bands. Standard pulse-compression methods were applied to the enlarged band of spectral data to provide a superresolved range profile of the target.

These UWB processing concepts were demonstrated by using simulations and static-range data. We showed that it was possible to accurately estimate a target's UWB response when the radar measurements fill only a small fraction of the total processing bandwidth. The practical payoff of this technology is that radar measurements need not be taken over the full UWB processing interval; signal processing can be used to a certain extent to compensate for any missing data. Another important benefit of UWB processing is that the α exponents of individual scattering centers can be more accurately estimated. This accuracy helps us to better identify the scattering centers that make up a target, which significantly improves our analysis and understanding of the target.

Suggestions for Future Research

Many unresolved issues in UWB processing of sparse-subband measurements remain. The uniqueness of our nonlinear optimization process, the accuracy of the initial pole estimates, and the performance versus band fill ratio (ratio of measured data to total processing interval) are important UWB processing concerns. While the nonlinear optimization process cross-correlates the subbands, it may be possible to obtain more resolved UWB signal models by better exploiting the cross-band correlation information during the initial pole estimation stage. We are currently investigating these issues and considering some potential real-time applications of this technology.

Acknowledgments

The authors would like to thank Michael Burrows of the Sensor Systems and Measurements group for providing radar-cross-section predictions for the monoconic reentry vehicle; we also would like to thank Mohamed Abouzahra of the Systems Engineering and Analysis group and Peter Kao of the Sensor Technology and Systems group for providing the static-range data that we used to demonstrate the applied aspects of ultra-wideband processing. This work was sponsored by the U.S. Space and Missile Defense Center.

REFERENCES

1. K.R. Roth, M.E. Austin, D.J. Frediani, G.H. Knittel, and A.V. Mrstik, "The Kiernan Reentry Measurements System on Kwajalein Atoll," *Linc. Lab. J.* **2** (2), 1989, pp. 247–276.
2. K.M. Cuomo, "A Bandwidth Extrapolation Technique for Improved Range Resolution of Coherent Radar Data," *Project Report CJP-60 Rev.1,* Lincoln Laboratory, 4 Dec. 1992, DTIC #ADA-258462.
3. S.L. Borison, S.B. Bowling, and K.M. Cuomo, "Super-Resolution Methods for Wideband Radar," *Linc. Lab. J.* **5** (3), 1992, pp. 441–461.
4. J.B. Keller, "Geometrical Theory of Diffraction," *J. Opt. Soc. Am.* **52** (2), 1962, pp. 116–130.
5. W.M. Steedly and R.L. Moses, "High Resolution Exponential Modeling of Fully Polarized Radar Returns," *IEEE Trans. Aerosp. Electron. Syst.* **27** (3), 1991, pp. 459–469.
6. E.F. Knott, J.F. Shaeffer, and M.T. Tuley, *Radar Cross Section: Its Prediction, Measurement and Reduction* (Artech House, Dedham, Mass., 1985), pp. 178–179.
7. S.Y. Kung, K.S. Arun, and D.V. Bhaskar Rao, "State-Space and Singular-Value Decomposition-Based Approximation Methods for the Harmonic Retrieval Problem," *J. Opt. Soc. Am.* **73** (12), 1983, pp. 1799–1811.
8. H. Akaike, "A New Look at the Statistical Model Identification," *IEEE Trans. Autom. Control* **19** (6), 1974, pp. 716–723.
9. M. Wax and T. Kailath, "Detection of Signals by Information Theoretic Criteria," *IEEE Trans. Acoust. Speech Signal Process.* **33** (2), 1985, pp. 387–392.
10. J. Rissanen, "Modeling by Shortest Data Description," *Automatica* **14** (5), 1978, pp. 465–471.
11. M. Wax and I. Ziskind, "Detection of the Number of Coherent Signals by the MDL Principle," *IEEE Trans. Acoust. Speech Signal Process.* **37** (8), 1989, pp. 1190–1196.
12. A.J. Barabell, J. Capon, D.F. DeLong, J.R. Johnson, and K.D. Senne, "Performance Comparison of Superresolution Array Processing Algorithms" *Project Report TST-72,* Lincoln Laboratory (9 May 1984, rev. 15 June 1998).
13. S.W. Lang and J.H. McClellan, "Frequency Estimation with Maximum Entropy Spectral Estimators," *IEEE Trans. Acoust. Speech Signal Process.* **28** (6), 1980, pp. 716–724.
14. R.O. Schmidt, "A Signal Subspace Approach to Multiple Emitter Location and Spectral Estimation," Ph.D. thesis, Stanford University, Stanford, Calif., 1981.
15. T.-J. Shan, M. Wax, and T. Kailath, "On Spatial Smoothing for Direction-of-Arrival Estimation of Coherent Signals," *IEEE Trans. Acoust. Speech Signal Process.* **33** (4), 1985, pp. 806–811.
16. A. Paulraj, R. Roy, and T. Kailath, "Estimation of Signal Parameters via Rotational Invariance Techniques—ESPRIT," *19th Asilomar Conf. on Circuits, Systems & Computers, Pacific Grove, Calif., 6–8 Nov. 1986,* pp. 83–89.
17. D.W. Tufts and C.D. Melissinos, "Simple, Effective Computation of Principal Eigenvectors and Their Eigenvalues and Application to High-Resolution Estimation Frequencies," *IEEE Trans. Acoust. Speech Signal Process.* **34** (5), 1986, pp. 1046–1053.
18. A. Moghaddar, Y. Ogawa, and E.K. Walton, "Estimating the Time-Delay and Frequency Decay Parameter of Scattering Components Using a Modified MUSIC Algorithm," *IEEE Trans. Antennas Propag.* **42** (10), 1994, pp. 1412–1418.
19. C.-W. Ma and C.-C. Teng, "Detection of Coherent Signals Using Weighted Subspace Smoothing," *IEEE Trans. Antennas Propag.* **44** (2), 1996, pp. 179–187.
20. W.H. Press, S.A. Teukolsky, W.T. Vetterling, and B.P. Flannery, *Numerical Recipes in C: The Art of Scientific Computing,* 2nd ed. (Cambridge University Press, Cambridgeshire, U.K., 1992).

KEVIN M. CUOMO
is a senior staff member in the Sensor Systems and Measurements group, where he specializes in the development of advanced signal processing methods for high-resolution radar. He has developed and implemented various radar imaging techniques, including extended coherent processing (ECP) to generate high-resolution three-dimensional radar images, and bandwidth extrapolation (BWE) to improve the range resolution of coherent radar returns. He has authored several technical papers and reports in the areas of superresolution data processing and applications of chaotic dynamical systems for secure communications. Recent efforts include the development of ultra-wideband processing techniques for mutually cohering and coherently combining sparse multispectral/multisensor radar measurements. Before joining Lincoln Laboratory in 1988, he was a member of the research staff at Calspan Corporation.

Kevin received B.S. (magna cum laude) and M.S. degrees in electrical engineering from the State University of New York (SUNY) at Buffalo, and a Ph.D. degree in electrical engineering from MIT in 1993. While attending SUNY at Buffalo, he was awarded Departmental Honors and was the recipient of a University Fellowship and a Hughes Fellowship. He is a member of Tau Beta Pi, Eta Kappa Nu, and Sigma Xi.

JEAN E. PIOU
is a staff member in the Sensor Systems and Measurements group and works on superresolution techniques related to radar target identification and imaging. His research interests include estimation theory and application, and eigenstructure assignment for multivariable stochastic systems. Before joining Lincoln Laboratory in 1995, he taught at City College of New York (CCNY) and the State University of New York (SUNY) at Binghamton, where he held visiting and assistant professorships, respectively.

Jean received B.S. degrees in applied mathematics and electrical engineering from the Université d'Etat d'Haiti, and M.S. and Ph.D. degrees in electrical engineering from the City University of New York (CUNY). He has published several technical papers in the areas of eigenstructure assignment for flight control systems.

JOSEPH T. MAYHAN
leads the Sensor Systems and Measurements group. Since joining Lincoln Laboratory in 1973, he has worked in the areas of satellite communications antennas, adaptive antenna design and performance evaluation, spatial spectral estimation that uses multiple-beam antennas, electromagnetic scattering from actively loaded targets, radar system design, and radar data analysis. He served two four-year tours at the Laboratory's Kwajalein field site in the Marshall Islands—the first as leader of the ALTAIR deep-space tracking radar and the second as site manager of the Lincoln Program at Kwajalein.

Joseph received a B.S. degree in electrical engineering from Purdue University, Lafayette, Indiana, and M.S. and Ph.D. degrees in electrical engineering from The Ohio State University in Columbus. Upon graduation, he worked on reentry systems analysis for Avco Corporation in Wilmington, Massachusetts. In 1969, he joined the faculty of the University of Akron in Ohio as an associate professor of electrical engineering.

Joseph has published extensively in the areas of nonlinear interactions of electromagnetic waves in plasma media, adaptive antenna design, spectral-estimation techniques, and electromagnetic scattering. He received the R.W.P. King award for papers published in the *IEEE Transactions on Antennas & Propagation.*